


RESEARCH ARTICLE

10.1029/2019MS001721

Key Points:

- Subgrid mesoscale eddy fluxes and velocity scales are diagnosed as a function of length scale using a spatial filtering approach
- In the presence of topography, subgrid-scale (SGS) eddy fluxes contain a strong standing component
- SGS eddy fluxes are modeled as a diffusion of planetary potential vorticity, and an empirical model of diffusivity is constructed

Correspondence to:

 S. Khani,
 skhani@uw.edu

Citation:

Khani, S., Jansen, M. F., & Adcroft, A. (2019). Diagnosing subgrid mesoscale eddy fluxes with and without topography. *Journal of Advances in Modeling Earth Systems*, 11, 3995–4015.
<https://doi.org/10.1029/2019MS001721>

Received 19 APR 2019

Accepted 29 OCT 2019

Accepted article online 8 NOV 2019

Published online 8 DEC 2019

Diagnosing Subgrid Mesoscale Eddy Fluxes With and Without Topography

Sina Khani^{1,2} , Malte F. Jansen³ , and Alistair Adcroft^{1,4}

¹Program in Atmospheric and Oceanic Sciences, Princeton University, Princeton, NJ, USA, ²Applied Physics Laboratory and School of Oceanography, University of Washington, Seattle, WA, USA, ³Department of Geophysical Sciences, University of Chicago, Chicago, IL, USA, ⁴NOAA Geophysical Fluid Dynamics Laboratory, Princeton, NJ, USA

Abstract General circulation models use subgrid-scale (SGS) parameterizations to represent the effects of unresolved mesoscale eddies on large-scale motions. Most of the current SGS parameterizations are based on a theoretical understanding of transient eddies, where the mean flow is a temporal average. In this work, we use a spatial filtering analysis to better understand the scale-dependent characteristics of the SGS fluxes. Specifically, we apply the filtering approach to diagnose SGS eddy volume fluxes and eddy velocity scales in a hierarchy of model configurations from a flat bottom channel to an idealized Southern Hemisphere. Importantly, SGS volume fluxes include significant contributions from standing meanders; unlike for transient eddies, the vertically integrated SGS volume flux does not necessarily integrate to 0. To accommodate net vertically integrated eddy fluxes, we define a SGS eddy diffusivity based on planetary potential vorticity (PV) diffusion. We diagnose the transient and standing contributions to SGS fluxes and associated effective diffusivities. In the presence of bottom topography or continental barriers the standing component of the PV diffusivity becomes dominant at large filter scales in the westerly wind region, while the transient component remains dominant in the easterly wind region. Our results suggest that the diagnosed PV diffusivity can be parameterized using mixing length theory based on *a priori* estimates of SGS velocity and length scales.

1. Introduction

Mesoscale eddies strongly influence the large-scale ocean circulation. These energetic eddies have horizontal scales of tens to a few hundred kilometers and play a crucial role in the transport of heat and tracers in the ocean (e.g. Hallberg & Gnanadesikan, 2006; McWilliams, 2008). Mesoscale eddies are ubiquitous but are especially prevalent near separated western boundaries and strong fronts. In the Southern Ocean, mesoscale eddies are responsible for the poleward transport of heat and equatorward transport of ocean bottom water across the Antarctic Circumpolar Current (McWilliams, 2008; Thompson, 2008). In numerical ocean models, a grid spacing Δ much smaller than the local Rossby radius of deformation is required to fully resolve the mesoscale eddies (Hallberg, 2013). In coarser resolution models, including many climate models, the effects of these eddies on the resolved large-scale motions have to be represented using subgrid-scale (SGS) parameterizations. Ideally, such a SGS model in non-eddy-permitting ocean models would be able to correctly capture eddy fluxes and their interactions with the large-scale ocean circulation.

Noneddycoarse resolution ocean models generally use the Gent and McWilliams (1990, hereafter GM) parameterization to represent the extraction of available potential energy (APE) from the large-scale flow via eddy volume fluxes. The GM diffusivity employed for the parameterization of this process can be formulated to depend on properties of the resolved flow (e.g. Danabasoglu & Marshall, 2007; Visbeck et al., 1997). At eddy-permitting resolution, the most energetic eddies are partially resolved. Here, a resolution aware scheme seems necessary to parameterize the effects of unresolved eddies. In addition to transient eddies, SGS transport can be due to unresolved standing meanders (see e.g. Mazloff et al., 2013; Treguier & McWilliams, 1990; Wolff, Maier-Reimer, & Olbers, 1991), which can include a wider range of lateral scales. Therefore, SGS parameterizations may need to be resolution aware even at noneddycoarse resolutions in order to account for standing meanders. The importance of grid spacing on parameterizations of mesoscale eddies in ocean models has long been considered in the formulation of momentum flux closures (e.g. Leith, 1996; Fox-Kemper & Menemenlis, 2008; Smagorinsky, 1963) but has only recently started to receive increasing attention in the formulation of the GM parameterization (e.g. Bachman et al., 2017; Hallberg, 2013). Resolution dependence

©2019. The Authors.

This is an open access article under the terms of the Creative Commons Attribution License, which permits use, distribution and reproduction in any medium, provided the original work is properly cited.

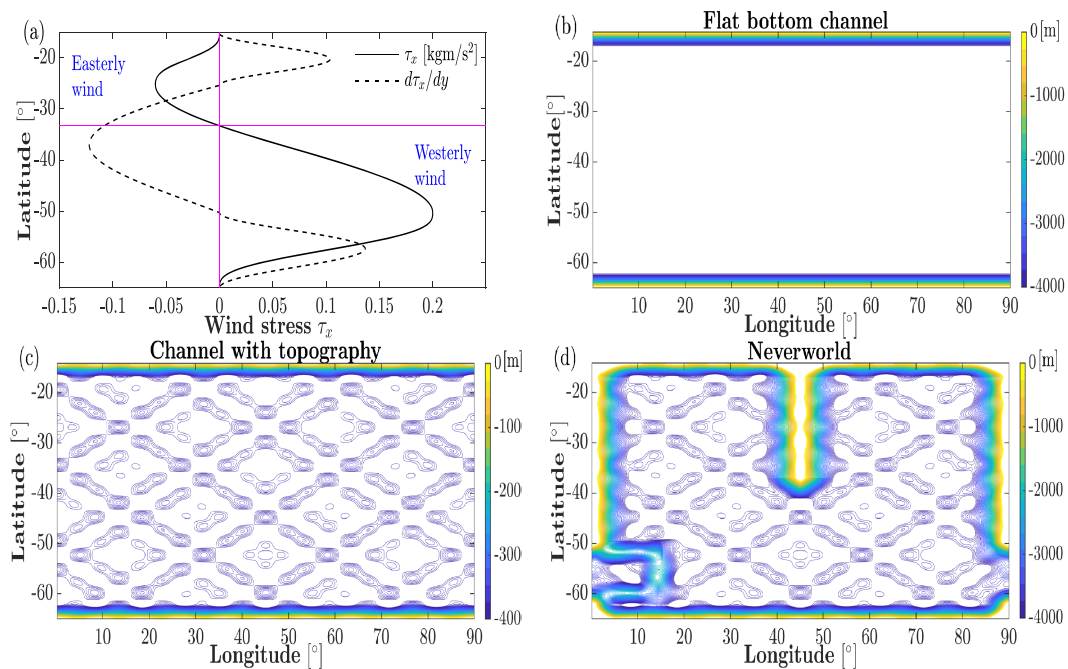


Figure 1. (a) Latitude-dependent wind stress. Ocean bathymetry in (b) flat bottom channel, (c) channel with bottom topography, and (d) Southern Hemisphere sector (Neverworld).

has also been studied in the context of SGS parameterizations in other types of turbulent flows in the atmosphere and ocean (e.g., atmospheric boundary layers Porté-Agel et al., 2000, buoyancy-driven turbulence Moeng & Sullivan, 1994, stratified turbulence Khani & Waite, 2015), and insights from these studies can be leveraged to tackle the problem of ocean mesoscale eddy parameterization.

A practical approach toward developing a scale-aware SGS mesoscale eddy parameterization is to directly study the characteristics of mesoscale eddy fluxes in high-resolution ocean models. Eddy fluxes in idealized high-resolution ocean models and satellite observations have been studied by Smith and Marshall (2009), Abernathey et al. (2010), Ferrari and Nikurashin (2010), and Abernathey et al. (2013), for example. In these studies, eddy fluxes are usually based on correlations of deviations from a time mean where only transient eddies are considered or correlations of deviations from a zonal mean where the entire spectrum of standing eddies is also included. These eddy fluxes by construction assume a binary definition of the flow field into mean and eddies and hence cannot capture the scale-dependent nature of SGS fluxes. Berloff (2005) studied scale-dependent eddy fluxes for a quasi-geostrophic flow in an idealized flat bottom box. They developed a simple coarse-graining method, in which the velocity and potential vorticity (PV) from an eddy-resolving simulation are coarse-grained, and the SGS eddy fluxes are calculated by subtracting the filtered PV flux from the total flux. They applied the computed SGS eddy flux as an eddy-forcing term in a noneddyng simulation to represent the effects of mesoscale eddies (Berloff, 2005). Building on this work, Berloff (2018) employed a spatial-scale decomposition method with a filter size similar to the scale of the baroclinic eddies to develop a deterministic mesoscale eddy parameterization. The spatial filtering approach has also been used to diagnose the cascade of energy across scales in the ocean (Aluie et al., 2018). Related approaches are widely applied in large-eddy simulation (LES) modeling, where effective SGS momentum fluxes are measured by applying a filtering operator to the results of direct numerical simulations (see e.g., Khani & Waite, 2016, where a similar methodology is employed in stratified turbulence).

Following the LES approach, we here diagnose SGS mesoscale eddy fluxes as a function of scale by applying a spatial filter to the results of eddy-resolving simulations in an idealized primitive-equation ocean model. The SGS eddy fluxes are calculated by subtracting the fluxes computed from the product of the filtered quantities from the filtered total fluxes. SGS eddy fluxes in this approach are filter scale dependent and include all unresolved motions, both transient and standing. This a priori approach [In the context of LES, an a priori approach refers to diagnosing SGS fluxes by employing an explicit filtering operator to the results of high-resolution simulations] provides important information about properties of unresolved motions,

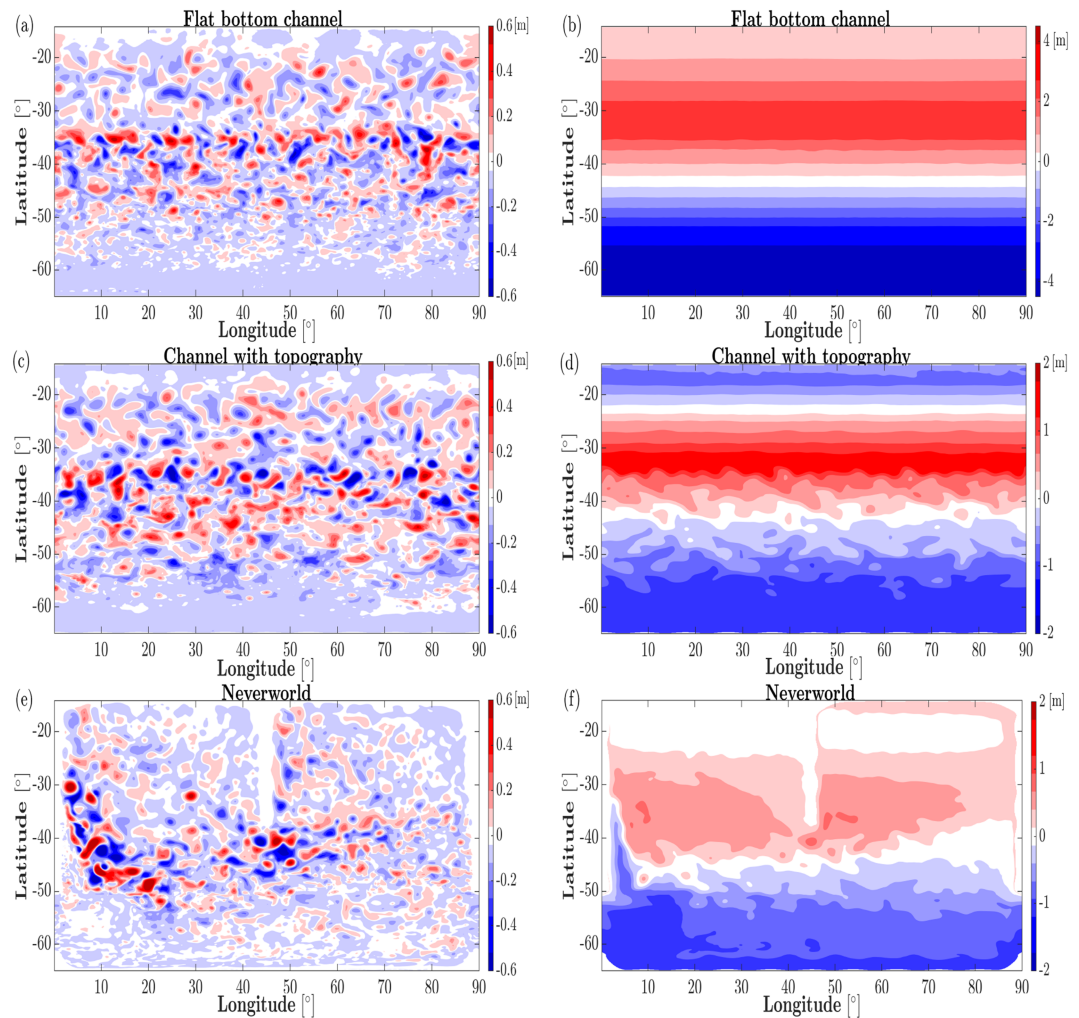


Figure 2. Sea surface height (SSH) anomaly at time $t = 75$ year (left panels) and SSH mean over the last 10 years of the simulations (right panels) for (a, b) flat bottom channel, (c, d) channel with bottom topography, and (e, f) Neverworld configurations.

including characteristics of SGS eddy fluxes and the effects of eddy transport on the large-scale ocean circulation. Here, we focus on eddy volume fluxes, which are typically modeled using the GM parameterization. We apply a box filter to high-resolution eddy-resolving simulations in a hierarchy of models from a flat bottom channel to an idealized Southern Hemisphere configuration. Section 2 describes the model setups, and gives a general overview of the simulations. The Reynolds-averaged and SGS transports are described in sections 3 and 4, respectively. In section 5, we discuss the diagnosed SGS eddy diffusivity and provide an interpretation in terms of a mixing length argument. Conclusions are given in section 6.

2. Model Setup

We use the latest generation of the Modular Ocean Model (MOM6) code (see GitHub repositories: github.com/NOAA-GFDL/MOM6 and github.com/sinakhani/Neverworld) in a strictly adiabatic configuration, which integrates to a full equilibrium in 100 years of simulation time. The model uses six constant density layers with $\rho = 1,025.5, 1,027, 1,027.5, 1,027.8, 1,028$, and $1,028.1 \text{ [kg/m}^3]$ from top to bottom, respectively. The initial layer thicknesses from top to bottom are, respectively, 150, 250, 600, 1,000, 1,000, and 1,000 [m]. The domain spans latitudes on a sphere from 65°S to 15°S and longitudes from 0° to 90° and is reentrant in the zonal direction. A turbulent circulation is driven by a latitude-dependent and zonally symmetric wind stress that is distributed across the top 20 [m] of the model (Figure 1a). The wind stress

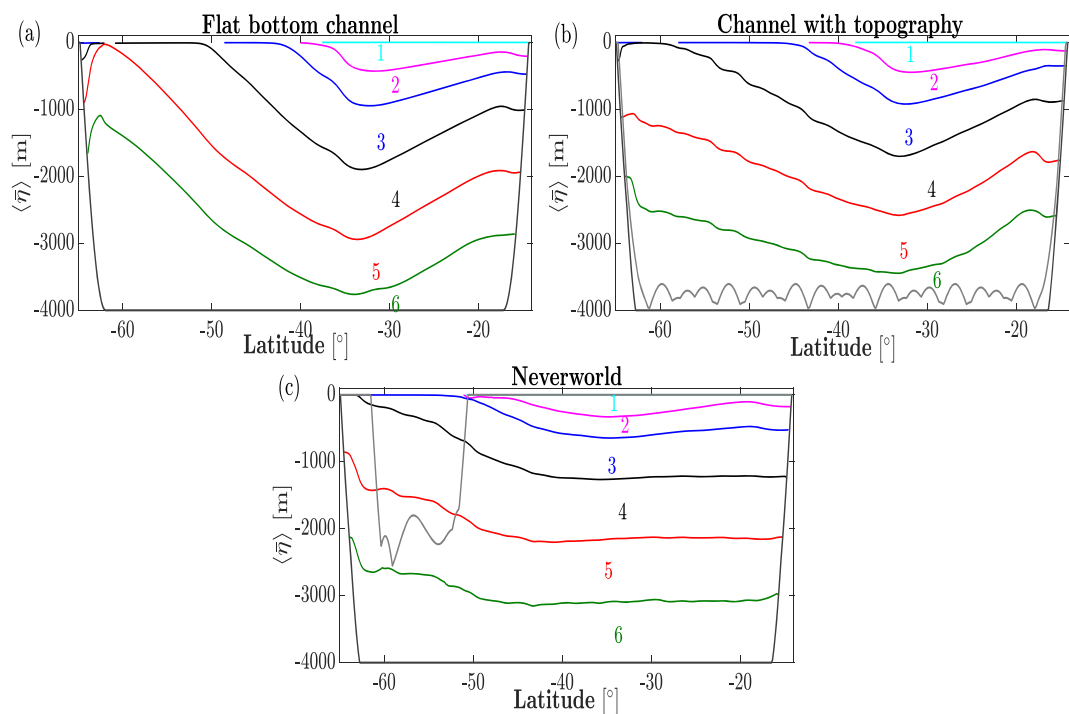


Figure 3. Time and zonally averaged density surfaces (isopycnals) for (a) flat bottom channel, (b) channel with bottom topography, (c) Neverworld. The gray lines show the shallowest and deepest topography at the bottom of the ocean, and time averaging has been performed over the last 10 years of simulations.

is easterly at low latitudes (near the equator) and westerly at middle to high latitudes. Three configurations for the ocean bathymetry are considered: a flat bottom channel (Figure 1b), a channel with bottom topography (Figure 1c) and a Southern Hemisphere-like idealized continental configuration, which we call “Neverworld” (Figure 1d).

We have performed eddy-rich simulations with a horizontal resolution of $(1/8)^\circ$ for all configurations. An additional $(1/16)^\circ$ simulation was performed in the Neverworld configuration to confirm that the results do not change significantly in finer resolution simulations. The Coriolis parameter $f = 2\Omega \sin \theta$, where $\Omega = 7.2921 \times 10^{-5}$ [s⁻¹] and θ is the latitude in degree. Note that all domains are in the Southern Hemisphere.

2.1. Overview of Simulations

All three simulations develop a turbulent flow field, illustrated via sea surface height (SSH) in Figure 2 (anomaly and mean SSH are shown in the left and right panels, respectively). Mesoscale structures are visible in all SSH anomalies. The mean SSH shows mostly larger-scale features, although a clear imprint of bottom topography is seen in the channel with topography and Neverworld simulations, particularly in the westerly wind-stress region. In channel configurations, transient mesoscale eddies are most prominent just south of the latitude where the wind direction changes sign (33° S) while the Neverworld configuration reveals strong mesoscale eddies in the Southern Ocean area and near western boundaries, as well as the tip of the short continent (at 45° E), where features similar to Aghulas rings are formed.

Density surfaces (isopycnals) are tilted by the Ekman pumping (see Figure 3). The sloped isopycnals indicate APE in the system, which is released via baroclinic instability. The isopycnal slopes are significantly shallower in the channel with topography compared to the flat bottom channel case (see panels a,b in Figure 3), which is evidence for a more efficient extraction of large-scale APE when bottom topography is present (see e.g. Abernathey & Cessi, 2014; Mazloff et al., 2013). In the Neverworld configuration, isopycnal slopes in the Southern Ocean are even shallower and isopycnals in the basin region to the north are almost flat (Figure 3c)—consistent with the presence of topographic barriers blocking zonal geostrophic flow.

Since our simulations are entirely adiabatic, no isopycnal overturning circulation can exist once a statistically steady state is reached. As a result, the meridional geostrophic transport (including mean and eddy contributions) exactly balances the wind-driven circulation (Ekman transport), so that the time-averaged

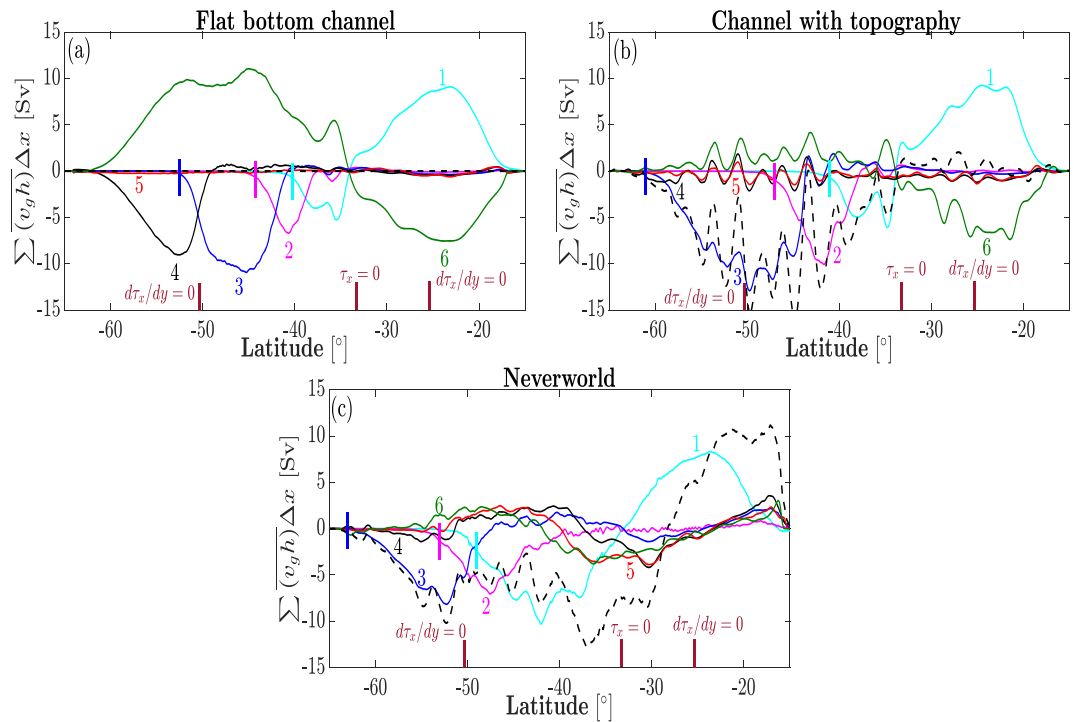


Figure 4. Time-averaged and zonally integrated geostrophic meridional volume transport for (a) flat bottom channel, (b) channel with bottom topography and (c) Neverworld. Layers from top to the bottom are numbered from 1 to 6, respectively, the black dashed line shows the vertical sums of the geostrophic volume transports over the water column, and the small vertical lines show the location where a layer vanishes and the layer beneath is exposed to the surface. Time averaging has been performed over the last 10 years of simulations. The latitudes of zero wind and zero curl crossing are indicated. Note that $1 \text{ [Sv]} = 10^6 \text{ [m}^3/\text{s]}$.

and zonally averaged total meridional transport $\langle \bar{v}h \rangle$ is exactly zero for each density layer (the bar sign $\bar{\cdot}$ and angle bracket $\langle \cdot \rangle$ denote time and zonal averaging, respectively; v is the meridional velocity, and h is the layer thickness). In the following we will focus on the geostrophic transport, noting that the ageostrophic transport is exactly equal and opposite. The meridional geostrophic transport $\langle v_g h \rangle$ (where v_g representing the geostrophic velocity, calculated using the gradient of the Montgomery potential) is confined mostly to the top and bottom layers (Figure 4a), where it balances the Ekman transport. Note that layers outcrop so the top most layer changes with latitude. In the flat bottom channel, the near-surface and abyssal transports balance, leading to no net meridional geostrophic transport. This balance changes in the presence of topography, where a net geostrophic transport can be maintained and related to the bottom form drag (dashed lines in Figure 4; and Johnson and Bryden 1989).

Figure 5 shows the eddy kinetic energy spectra, which are computed using the deviation from the time-averaged and zonally averaged velocity, at the surface in the Antarctic Circumpolar Current region. The energy spectra show an approximately -3 power law in the inertial subrange, which indicates a forward enstrophy cascade below 200 [km]. For scales larger than $\sim 4^\circ$, the eddy kinetic energy spectra are flat, indicating a maximum eddy scale of around 4° .

3. Reynolds Averaged Transport

Existing parameterizations of eddy fluxes are motivated mostly by our physical understanding of transient eddies. Following many previous studies on eddy fluxes, we start by decomposing the time-averaged meridional geostrophic volume transport $\bar{v}_g h$ into the mean flow and transient components using a Reynolds averaging approach

$$\bar{v}_g h = \bar{v}_g \bar{h} + \bar{v}'_g h', \quad (1)$$

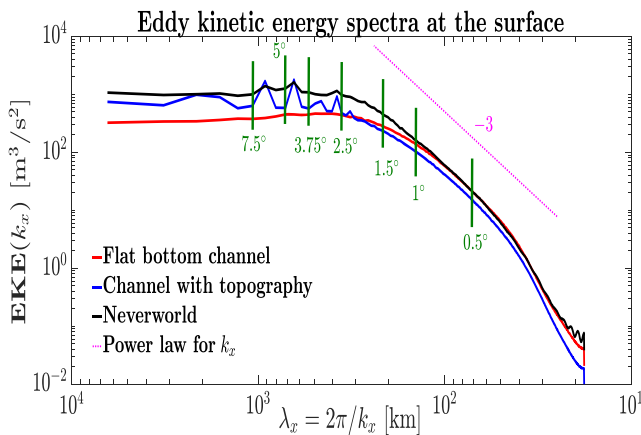


Figure 5. Time-averaged surface eddy kinetic energy spectra as a function of zonal wavelength. The spectra are averaged over the latitude 60°S to 40°S, a latitude band for the channel location in the Neverworld configuration. Time averaging has been performed over the last 10 years of simulations. The vertical lines show the Nyquist wavelengths corresponding to the horizontal filter scales, which will be discussed in section 4. Notice that all spectra are taken as a function of zonal wavenumber, but for convenience the horizontal axis has been labeled to indicate the corresponding wavelength (in km) at a latitude of $\theta = 50^\circ\text{S}$. (At higher latitudes the same wavenumber corresponds to a somewhat smaller wavelength, while at lower latitudes it corresponds to a somewhat longer wavelength.)

in the region with easterly wind, while standing flows are dominant in the westerly wind region. The importance of topography and associated standing meanders in the region with westerly wind is consistent with the mean SSH field in Figure 2, where the influence of topography structures is apparent in the westerly wind region while not seen in easterly wind region. Note that the dominance of standing meanders in the westerly region is not because the westerly wind is stronger than the easterly wind (as shown in Figure 1a). We have tested this argument by reversing the wind stress sign, in which case the easterly wind becomes stronger, but standing meanders are still dominant in westerly wind region (not shown).

In the Neverworld configuration, the layer-by-layer volume transports are significantly more complicated than those in the channel configurations because of the continental barriers, but the transient component of the volume transports is generally much smaller than the standing component, except in the top layer of the easterly wind region (see Figures 6e and 6f). Since there are continental barriers, the surface Ekman transport is balanced mostly by a geostrophic return transport in the interior, whose vertical integral is therefore roughly equal and opposite to the Ekman transport.

Overall, while transient eddies balance the wind-driven circulation in the flat bottom channel configuration (Figures 6a and 6b), the time mean geostrophic transport plays the dominant role in balancing the westerly wind stress circulation in the presence of bottom topography and/or continents (Figures 6c–6f). The crucial role of the time mean geostrophic transport even in the “Drake Passage” region is at least qualitatively consistent with the results of Mazloff et al. (2013).

It is also worth noting that, since the bottom form drag has no transient contribution, the vertical integral of the time and zonally averaged transient geostrophic eddy fluxes is always identically 0; that is,

$$\sum_{bot.}^{top} \langle v'_g h' \rangle = 0. \quad (2)$$

This integral is shown by the black dashed lines in Figure 6 for the left panels. The geostrophic mean flow transport, however, can have a nonzero depth integrated transport in the presence of bottom topography (right panels). We will return to this point in the discussion of the SGS transport in later sections.

where the prime sign denotes deviations from the time average. We will later compare these components with the SGS meridional volume transport. The time averaged and zonally averaged transient $\langle v'_g h' \rangle$ and mean $\langle \bar{v}_g \bar{h} \rangle$ geostrophic meridional volume transports are shown in Figure 6. In the flat bottom channel case, the wind-driven circulation is balanced exclusively by transient eddies because there are no time mean geostrophic meridional flows (Figures 6a and 6b). In the presence of bottom topography, the time mean transport can be nonzero and balances most of the wind-driven circulation in the region with westerly wind, while the transient eddy transport remains dominant in the easterly wind region. Note that the time mean flow component includes both contributions from the time and zonal mean geostrophic transport, as well as contributions from standing eddies. A further decomposition of the standing transport into an Eulerian mean overturning and standing eddy contributions is not straightforward in a stacked shallow water model, and is not attempted here.

We speculate that the qualitatively different role of the standing flow contribution in the westerly and easterly wind regions results from the difference in the PV structure and its effects on the nature of the baroclinic instability. Deeper (Phillips-type) modes, which are more influenced by bottom topography, occur in the westerly wind region, while shallower (Charney-type) modes are supported in the region with easterly wind (e.g. Tulloch et al., 2011). Moreover, the upper layers increasingly vanish in the westerly wind region, and hence, there is less stratification, which is also expected to lead to deeper and less surface intensified modes. As a result, transient eddies dominantly balance the wind-driven circulation

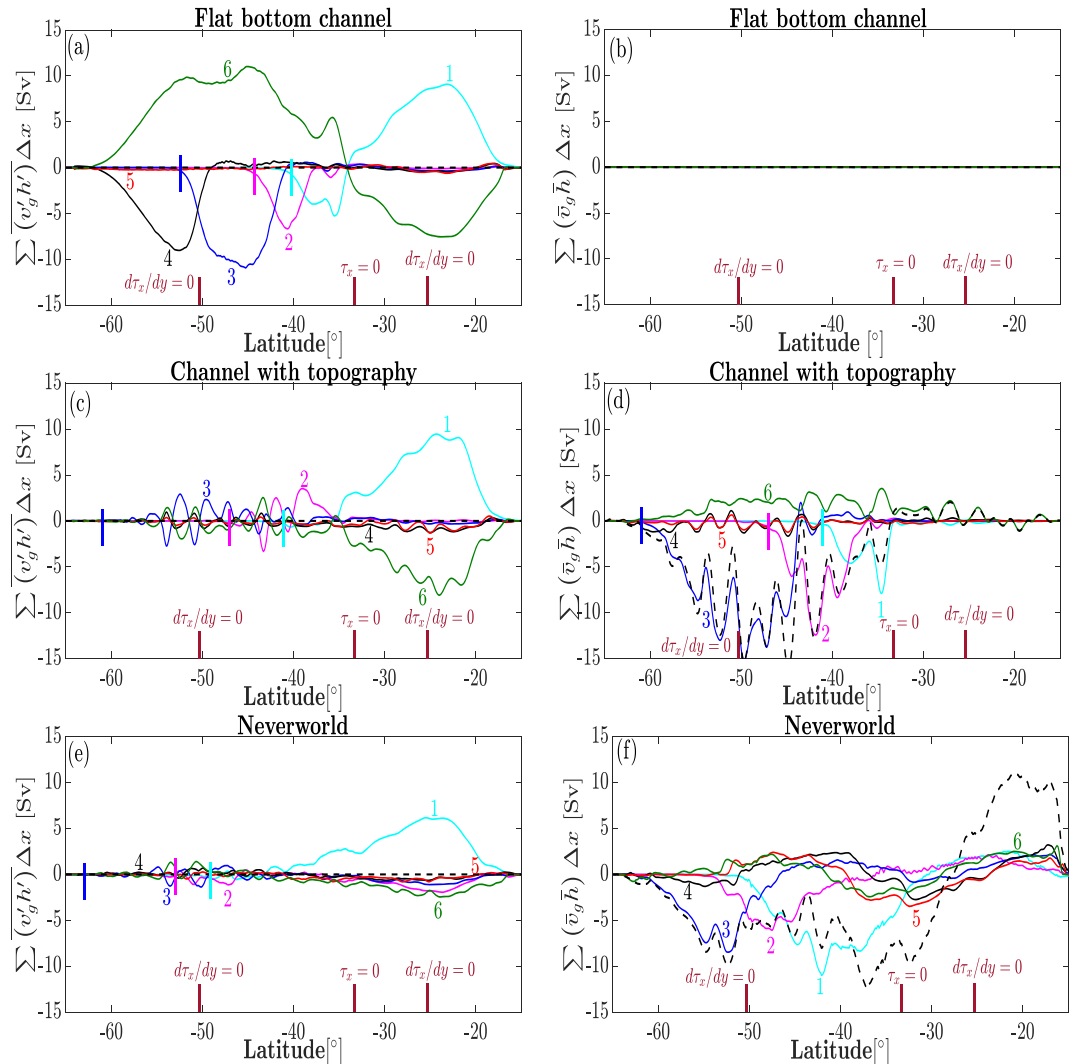


Figure 6. As Figure 4 but showing the transient (left panels) and mean (right panels) components of the geostrophic meridional volume transport.

4. Scale-Dependent Decomposition

We introduce a spatial filtering approach to diagnose SGS eddy fluxes in the above-mentioned models. We apply a filtering function to the high-resolution eddy-rich solutions and decompose turbulent motions into the “resolved” and “SGS” components with respect to the filter scale. For a variable m , we define the filtered variable as

$$\tilde{m}(i, j, t) = \sum_{i^*} \sum_{j^*} G_{\Delta_f}(i - i^*, j - j^*) m(i^*, j^*, t) A(i^*, j^*), \quad (3)$$

where $A(i, j)$ is the area of a grid cell, G_{Δ_f} is a top-hat filtering function given as

$$G_{\Delta_f}(i - i^*, j - j^*) = \begin{cases} \frac{1}{A_{\Delta_f}}, & \text{if } |i - i^*| \leq \frac{N_f}{2} \text{ and } |j - j^*| \leq \frac{N_f}{2} \\ 0, & \text{otherwise.} \end{cases} \quad (4)$$

Here the tilde sign $\tilde{\cdot}$ denotes a filtered variable, $A(i, j)$ is the grid box area in the high-resolution reference simulation, and $A_{\Delta_f}(i, j)$ is the area of the filter stencil; $N_f = \Delta_f/\Delta$ where Δ_f is the filter scale and Δ is the nominal resolution of the reference simulation. Spatial filtering is not equivalent to Reynolds averaging; in particular, certain mathematical properties of Reynolds averages, such as $\bar{\bar{m}} = \bar{m}$ and $\bar{m}' = 0$, do not hold here, that is, $\tilde{m} \neq \bar{m}$ and $\tilde{m}' \neq 0$. This filtering approach is not as general as the approach for filtering on

a sphere introduced by Aluie (2019). For the diagnostics of interest for the current study we do not strictly require commutation with derivatives, and thus, a simple filtering approach that follows the native model grid is sufficient. In Appendix A, we show unfiltered, filtered and SGS surface velocities to illustrate that how the spatial filtering operates on a field.

In the LES approach, the SGS geostrophic volume transport and kinetic energy are

$$(\mathbf{u}_g h)_{sgs} = \widetilde{\mathbf{u}_g h} - \tilde{\mathbf{u}}_g \tilde{h}, \quad (5)$$

$$\frac{1}{2} (\mathbf{u}_g^2)_{sgs} = \frac{1}{2} (\widetilde{\mathbf{u}_g \cdot \mathbf{u}_g} - \tilde{\mathbf{u}}_g \cdot \tilde{\mathbf{u}}_g), \quad (6)$$

where $\mathbf{u}_g = (u_g, v_g)$ is the horizontal geostrophic velocity. We could alternatively define a SGS kinetic energy as the square of the SGS velocity

$$\frac{1}{2} (\mathbf{u}_g)^2_{sgs} = \frac{1}{2} (\mathbf{u}_g - \tilde{\mathbf{u}}_g) \cdot (\mathbf{u}_g - \tilde{\mathbf{u}}_g). \quad (7)$$

Although the definition in (6) is consistent with the definition of the SGS model and reflects the missing kinetic energy in the filtered solution, equation (7) provides the kinetic energy of the SGS velocity field. The main difference between these two SGS kinetic energy definitions is that the global average of SGS kinetic energy defined by equation (7) does not include the cross term between the filtered and SGS velocities, while the definition in (6) does (if we subtract equation (7) from equation (6) the residual is $2\tilde{\mathbf{u}}_g (\mathbf{u}_g - \tilde{\mathbf{u}}_g) + (\widetilde{\mathbf{u}_g^2} - \mathbf{u}_g^2)$). The first term captures correlations between the resolved and SGS velocities. The second term approximately vanishes upon temporal or spatial averaging for a sufficiently homogeneous flow). In the next section, we compare these two definitions of SGS kinetic energy.

We can further decompose the SGS geostrophic volume transport $\overline{(\mathbf{u}_g h)}_{sgs}$ into the transient and standing components, written as

$$\overline{(\mathbf{u}_g h)}_{sgs} = \overline{(\mathbf{u}_g h)}_{sgs}^{tr} + \overline{(\mathbf{u}_g h)}_{sgs}^{st}, \quad (8)$$

where the transient contribution is defined as the SGS component of the transient eddy flux:

$$\overline{(\mathbf{u}_g h)}_{sgs}^{tr} \equiv \left(\overline{\widetilde{\mathbf{u}_g h'}} - \overline{\widetilde{\mathbf{u}_g} \tilde{h}'} \right) \quad (9)$$

and the standing component is given by the remainder of the SGS flux:

$$\overline{(\mathbf{u}_g h)}_{sgs}^{st} \equiv \overline{(\mathbf{u}_g h)}_{sgs} - \overline{(\mathbf{u}_g h)}_{sgs}^{tr} \quad (10)$$

$$= \left(\overline{\widetilde{\mathbf{u}_g h}} - \overline{\widetilde{\mathbf{u}_g} \tilde{h}} \right) + \left(\overline{\widetilde{\mathbf{u}_g h'}} + \overline{\widetilde{\mathbf{u}_g} \tilde{h}} - \overline{\widetilde{\mathbf{u}_g} \tilde{h}'} - \overline{\widetilde{\mathbf{u}_g} \tilde{h}} \right), \quad (11)$$

If the time averaging and filtering operators commute, the second parenthesis on the right-hand side of equation (11) vanishes. While the operators do commute in the interior, they generally do not commute near the boundaries (see 4.1 below for more information). A similar decomposition can also be applied to the SGS kinetic energy.

We have applied the above SGS decomposition using different filter scales to the results of eddy-rich simulations, varying the filter widths across scales relevant for eddy-permitting to noneddyng ocean model resolutions. Notice that our filtering operator is unaware of the model grid (Mercator grid in our case): We average over a fixed number of grid points in latitudinal and longitudinal directions. An alternative approach can be to define a filter width based on the local deformation radius (as in e.g. Berloff, 2018). This approach can provide valuable physical insights but is less applicable to the problem of eddy parameterization in noneddyng ocean models. The Nyquist wavenumbers corresponding to the selected filter scales are indicated in the eddy kinetic energy spectra in Figure 5 (vertical green lines). The horizontal size of the largest mesoscale eddies is around 4° , where the upscale energy transfer ends (spectra become flat). We therefore focus on the SGS volume transport with $\Delta_f = 3.75^\circ$ (the scale of the eddies) to illustrate the characteristics of SGS eddy fluxes at noneddyng resolutions. Similar results are also obtained for larger filter widths.

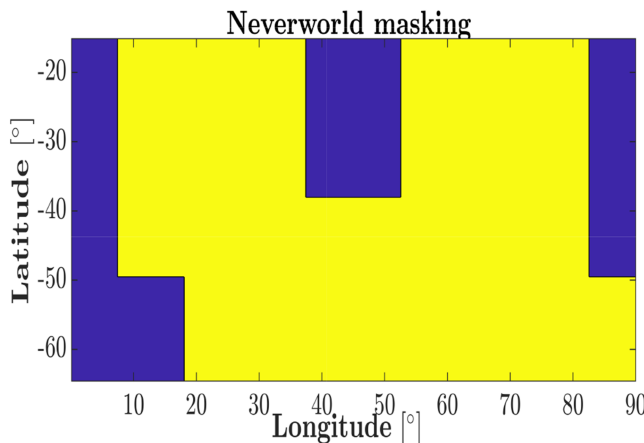


Figure 7. The Neverworld configuration mask, where the blue color shows the regions that are masked in our analysis of SGS eddy diffusivity and velocity.

We are not sure how to make a direct connection between the filtering scale and the actual grid spacing targeted by a parameterization. The numerics of ocean models generally require the solution to be smooth near the grid scale so that the effective resolution is coarser than the grid scale. We suggest that the filter scale applied to our eddy-rich solutions be interpreted as the effective resolution of an ocean model, which might be two to four times the grid spacing but may not be well defined for noneddying resolutions (Soufflet et al., 2016).

4.1. Treatments of Vanished Density Layers

In computing averages (be it in time or over a spatial filtering stencil) on isopycnal layers, care must be taken on how to treat isopycnal out and in-crops as well as land points (if included in the averaging domain). For the isopycnal layer thickness h , we can simply treat vanished layers as having zero thickness (consistent with the formulation of MOM6), and hence, the geostrophic thickness fluxes vanish similarly. However, to compute eddy and SGS fluxes, we have to define averages of the geostrophic velocity, which is somewhat less straightforward, particularly in the presence of bottom topography.

For surface outcrops, the definition of the geostrophic velocity (based on the gradient of the Montgomery potential) can readily be extended to the vanishing part of an isopycnal, where it simply yields the surface geostrophic velocity. For isopycnal in-crops with a sloping bottom boundary, the same approach can yield spurious large geostrophic velocities even for an ocean at rest (because the layer interface overlying a vanished layer follows the topographic slope, which leads to a gradient in the Montgomery potential). We therefore treat bottom in-crops as horizontal boundaries, beyond which physical quantities are not defined.

Spatially filtered fields near boundaries are defined by reducing the size of the spatial filtering stencil to avoid land points (or in-crops). In particular, at every grid point (i, j) , the local stencil size N_f in equation (4) is limited by the maximum value that ensures that no land points are included in the averaging. As a result, the shape of the filtering kernel remains unchanged but the filtering scale is reduced, such that the filtered field converges toward the full field and the SGS component vanishes near boundaries.

Since the choice of how to define filtered fields near boundaries will unavoidably affect the results, we minimize these effects when diagnosing eddy diffusivity and velocity scales in the Neverworld configuration by masking out regions around the topography (see Figure 7). While this means that we are missing some of the arguably most interesting regions, we do not think that SGS fluxes can be defined unambiguously near boundaries, and hence diagnosed diffusivities would not be robust in these regions.

4.2. Diagnosed SGS Velocity

Using the SGS kinetic energy $(1/2) \langle \mathbf{u}_g^2 \rangle_{sgs}$, we define the effective SGS velocity magnitude V_{sgs} as

$$V_{sgs} = \sqrt{\langle \mathbf{u}_g^2 \rangle_{sgs}}. \quad (12)$$

A second characteristic velocity magnitude is defined similarly for the alternative SGS kinetic energy definition $(1/2) \langle \mathbf{u}_g^2 \rangle_{sgs}^{st}$. We, furthermore, decompose the diagnosed SGS velocity scale into the transient and standing components using the following equations

$$\overline{\langle \mathbf{u}_g^2 \rangle_{sgs}}^{tr} = \left(\overline{\widetilde{\mathbf{u}'_g \mathbf{u}'_g}} - \overline{\mathbf{u}'_g} \overline{\mathbf{u}'_g} \right), \quad (13)$$

$$\overline{\langle \mathbf{u}_g^2 \rangle_{sgs}}^{st} = \overline{\langle \mathbf{u}_g^2 \rangle_{sgs}} - \overline{\langle \mathbf{u}_g^2 \rangle_{sgs}}^{tr}. \quad (14)$$

In order to present SGS velocities diagnosed as a function of filter scale, we separate the domain into two dynamically distinct regions (based on the easterly versus westerly wind stress) and compute area averages over each of these regions. Figure 8 shows the diagnosed SGS velocities at the surface (local top layer) in

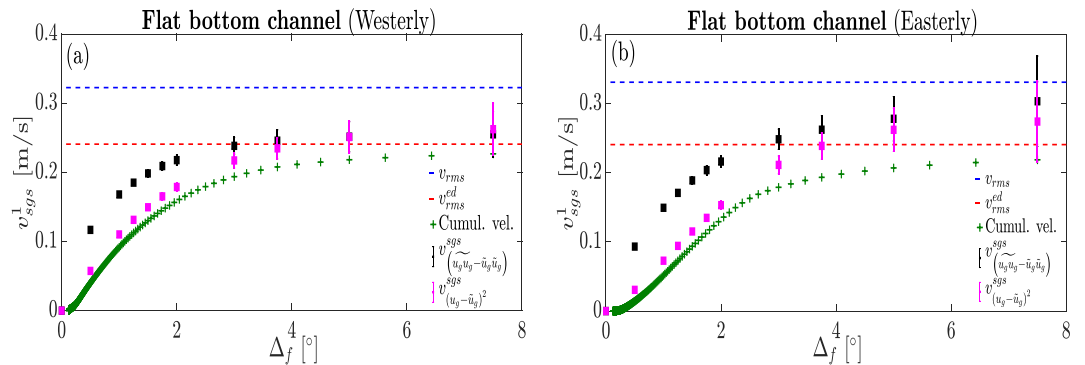


Figure 8. Area-averaged SGS velocity for the top layer $v_{sgs}^1 = \langle\langle \overline{V_{sgs}^1} \rangle\rangle$, where $\langle\langle \cdot \rangle\rangle$ denotes a horizontal average, versus the filter width for the flat bottom channel in (a) westerly wind (latitudes $\theta < -33.3^\circ$), and (b) easterly wind (latitudes $\theta \geq -33.3^\circ$). Black and magenta squares use the SGS kinetic energy definitions in equations (6) and (7), respectively. The blue and red dashed lines show the total and eddy r.m.s. velocities (where the eddy component is defined as deviations from the time and zonal mean). Green plus signs show the cumulative spectral eddy velocity (see the text for explanation). Time averaging is performed over the last 10 years of simulations. The procedure for calculating confidence intervals is given in D.1.

the flat bottom channel case based on the two definitions of SGS kinetic energy in equations (6 and 7) as a function of filtering scale. For comparison, we also compute a subscale velocity defined by integrating the eddy kinetic energy (EKE) spectrum from the corresponding Nyquist wavenumber $k_f = \pi/\Delta_f$ to the largest wavenumber. At small filter scales, the LES-based SGS velocity (as defined in equation (6)) is much larger than that defined by equation (7), but the two SGS velocities converge at large filter widths. When the scale of eddies is captured (i.e., $\Delta_f \gtrsim 3.75^\circ$), the diagnosed SGS velocities converge to values in between eddy and total root-mean-square velocities (Figure 8). This behavior demonstrates that the diagnosed SGS velocity has contributions of both eddy and mean velocities. The cumulative velocity from the EKE spectrum is close to the SGS velocity scale defined based on the EKE definition in (7). For the rest of this paper, we use the LES-based definition of SGS velocity given by equation (6) since this definition is consistent with the definition of SGS eddy fluxes as shown in equation (5). Notice that higher moment filtering kernels can be used to generate SGS kinetic energies that more closely reproduce the cumulative kinetic energy spectrum (Sadek and Aluie, 2018). However, the goal here is not to reproduce a spectral decomposition, but to analyze energy and flux components that cannot be represented in coarse resolution ocean models, and hence here we employ a simple box filter.

The volume-averaged SGS velocity, along with the transient and standing components, are shown in Figure 9. In channel configurations, the diagnosed SGS velocities increase from zero when $\Delta_f \equiv \Delta$ to a value around 0.12 [m/s] with westerly wind and 0.10 [m/s] with easterly wind when SGS velocities plateau around 4° (see Figures 9a–9d). In the Neverworld configuration, the SGS velocity converges to 0.08 [m/s] (westerly region) and 0.07 [m/s] (easterly region), which is smaller than those in channel configurations (see Figures 9e and 9f). This behavior shows that the SGS velocity reduces in the presence of basins and/or significant topography near Drake Passage. Note that the flat bottom channel case naturally has no standing SGS velocity component, and the total SGS velocity is the same as its transient component. The channel with topography and Neverworld cases both have transient and standing SGS velocity components, for which $v_{sgs}^2 = v_{sgs,tr}^2 + v_{sgs,st}^2$ (subscripts “tr” and “st” denote the transient and standing components, respectively). Overall, the transient component of the volume-averaged SGS velocity remains dominant in all cases and regions, although there is a significant standing contribution to the SGS velocity when topography is present (Figures 9c–9f).

4.3. SGS Eddy Transport

In this section, we describe the SGS meridional volume transport and volume-averaged diagnosed PV diffusivity that are computed by filtering the results of the eddy-resolving simulations.

We start by considering the zonally integrated SGS volume transport at a filter scale of $\Delta_f = 3.75^\circ$, where most of the transient eddies are removed from the resolved flow. In this case, the SGS geostrophic

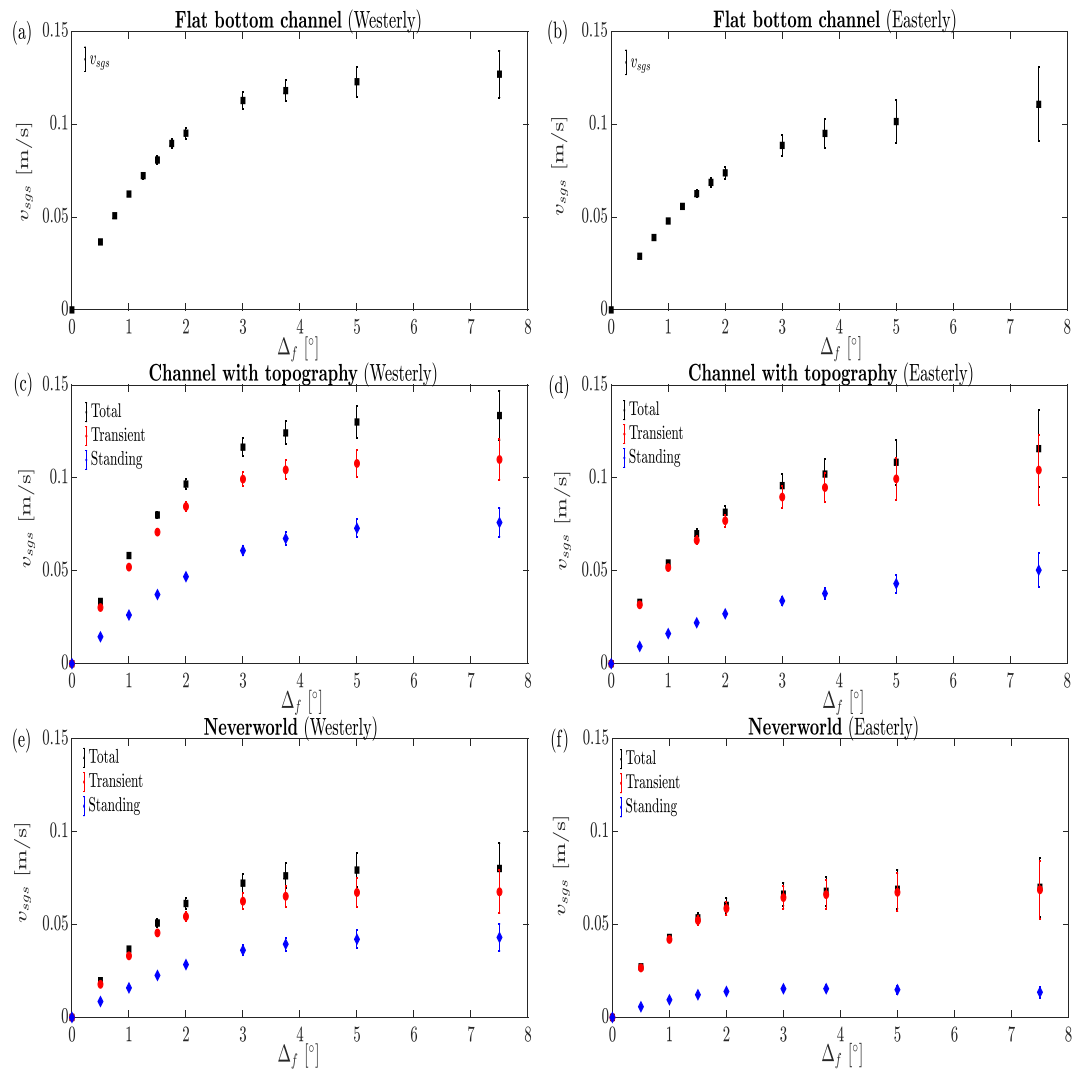


Figure 9. Diagnosed volume-weighted SGS velocity $v_{sgs} = \langle\langle\langle V_{sgs}\rangle\rangle\rangle$, where $\langle\langle\langle \cdot \rangle\rangle\rangle$ denotes a volume average, versus filter width with westerly wind (left panels) and easterly wind (right panels) for (a, b) flat bottom channel, (c, d) channel with bottom topography, and (e, f) Neverworld. Easterly and westerly winds include regions with latitudes $\theta \geq -33.3^{\circ}$ and $\theta < -33.3^{\circ}$, respectively, except the Neverworld configuration where the westerly region is restricted to $\theta < -50^{\circ}$ in order to isolate the dynamics in the reentrant channel region. Time averaging is performed over the last 10 years of simulations.

meridional volume transport in the flat bottom channel (Figure 10a) is very similar to the transient geostrophic meridional volume transport $\langle v'_g h' \rangle$ (shown in Figure 6a). These similarities are because the flat bottom channel case has no mean component (Figure 6b), and therefore, the resolved geostrophic meridional volume transport is negligible when all eddies are encompassed by the filter when $\Delta_f \gtrsim 3.75^{\circ}$ (Figure 10b). In the presence of bottom topography or continental barriers, the SGS geostrophic meridional volume transport is very different from the transient geostrophic volume transport in the westerly wind region, where it includes significant contributions from unresolved standing meanders, while they remain broadly similar in the easterly wind region (Figures 10c and 10e vs. Figures 6c–6f). Note also that, unlike for the transient eddy volume flux, the vertical integral of the SGS transport generally does not vanish in the presence of bottom topography. In the channel model, the zonally and vertically integrated SGS transport is directly related to the SGS form stress (see the discussion in Appendix B). The resolved volume transport remains relatively small in the channel with bottom topography in the region with easterly wind because the transport is dominated by transient eddies with scales smaller than the filter scale $\Delta_f = 3.75^{\circ}$. In the westerly wind region, the resolved meridional volume transport instead is not negligible as the standing meanders

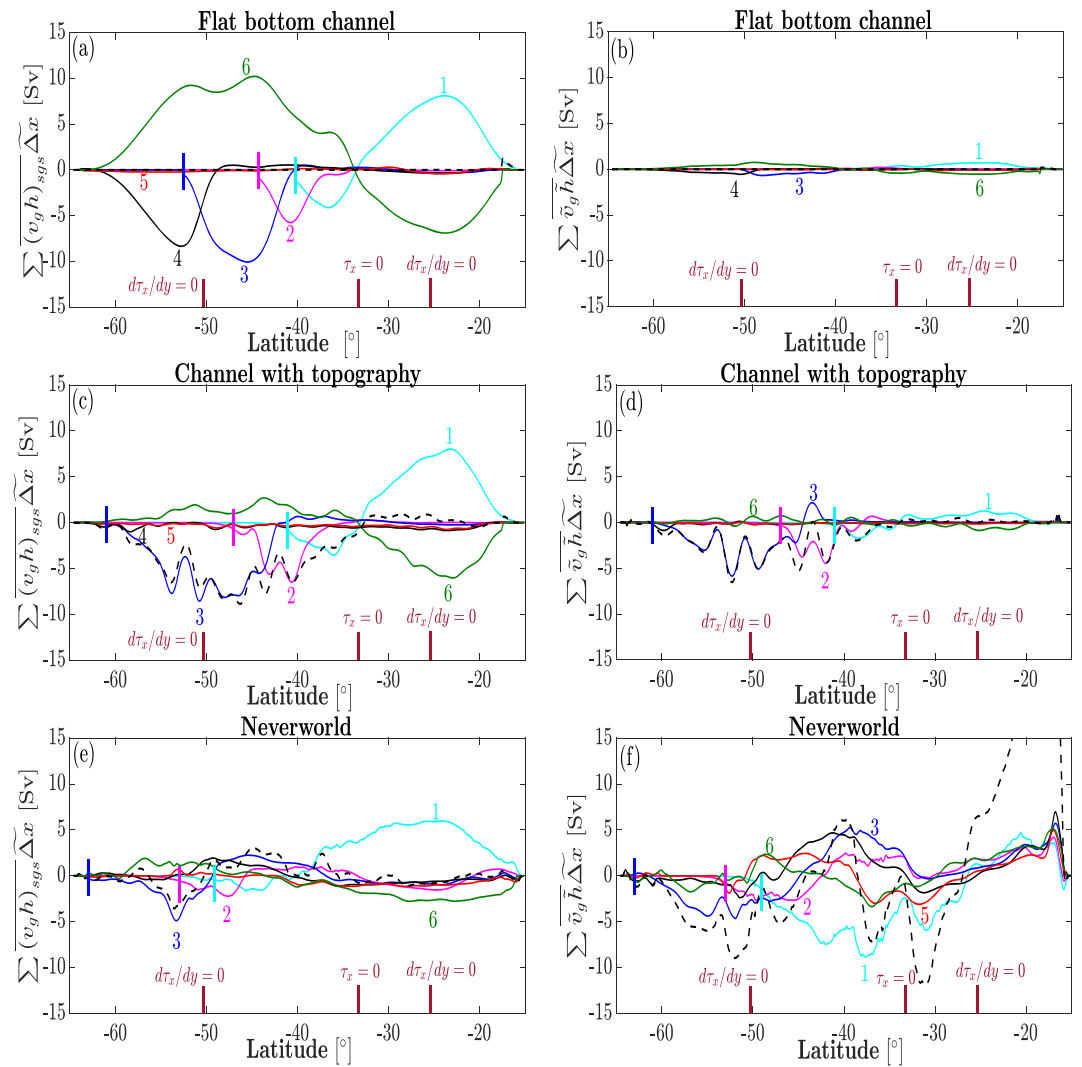


Figure 10. Time and zonally integrated SGS (left) and resolved (right) geostrophic volume transport with the filter scale $\Delta_f = 3.75^\circ$, for (a, b) flat bottom channel, (c, d) channel with bottom topography, (e, f) Neverworld. See also the caption of Figure 6.

can be partially resolved (Figures 10d). In the Neverworld configuration, the resolved geostrophic volume transport is generally larger than the SGS transport (Figures 10e and 10f), showing that the large-scale geostrophic transport plays a dominant role in the presence of continental barriers.

We further decompose the SGS geostrophic meridional volume transport into transient and standing components (shown in Figure 11). In the flat bottom channel, the SGS meridional volume transport again has no standing component because there are no standing meanders (see Figure 6b), and the SGS transport is entirely due to transient eddies (Figures 11a and 11b). In the channel with bottom topography, the transient SGS meridional volume transport is dominant in the easterly wind region, while the standing component is dominant with westerly wind (Figures 11c and 11d). This behavior is in line with the Reynolds average decomposition, in which transient eddies and mean flow are mainly dominant in the easterly and westerly regions, respectively (see Figures 6c and 6d). The Neverworld results are qualitatively similar to those in the channel with topography: The transient component of the SGS geostrophic volume transport is dominant in the easterly wind region, while the standing component dominates the westerly wind region (Figures 11e and 11f).

In summary, we see that the zonally averaged SGS geostrophic volume transport is primarily due to transient eddies in all configurations where the wind is easterly. In the region with westerly wind, however, the

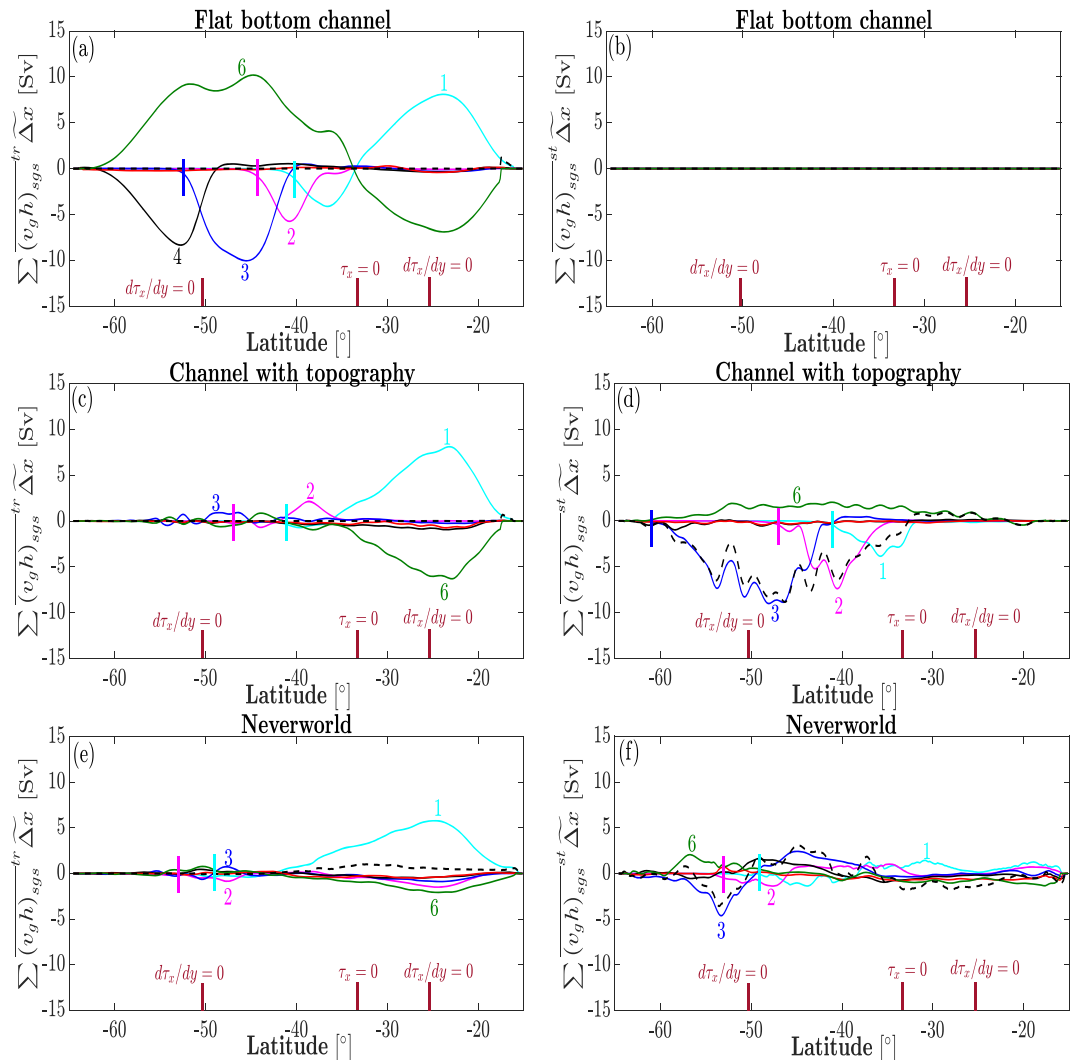


Figure 11. Time and zonally integrated transient (left) and standing (right) SGS geostrophic volume transport with the filter scale $\Delta_f = 3.75^\circ$, for (a, b) flat bottom channel, (c, d) channel with bottom topography, and (e, f) Neverworld. See also the caption of Figure 6.

presence of topography and/or continents results in large SGS volume transport due to unresolved standing meanders.

4.3.1. Defining a “Diffusivity” for Eddy Volume Fluxes

In noneddy and eddy-permitting ocean models, we are parameterizing the SGS volume transport. In most coarse resolution ocean models, the unresolved (eddy) volume transports are parameterized using the GM closure, in which the eddy volume flux is described by a stream function that is proportional to the isopycnal slope. In a stacked shallow water model the GM streamfunction is

$$\Psi_n \equiv - \sum_{k=n}^N \overline{(\mathbf{u}_g^k h^k)}_{sgs} \propto \nabla \bar{\eta}_n, \quad (15)$$

where η is the isopycnal layer interface height, n indicates the isopycnal, and $N = 6$ is the total number of layers. One implication of this formulation is that the vertically integrated volume transport is 0 because the free surface is essentially flat (i.e., $d\bar{\eta}_1/dy = 0$) relative to interior interfaces, so that the GM model yields $\sum_1^N \langle v_g h \rangle_{sgs} \simeq 0$. This constraint may be appropriate for transient eddy fluxes, but it is not consistent with our results for the full SGS fluxes in the presence of topography and/or land (see the black dashed lines in Figures 10 and 11). An important consequence of this inconsistency is that we can not unambiguously infer a GM diffusivity, as the SGS fluxes do not unambiguously define a streamfunction. To proceed, we here

instead consider a diffusive closure for planetary PV, which is unambiguously defined. A PV diffusivity has repeatedly been suggested as a more physical closure than GM (e.g. Greatbatch, 1998; Treguier et al., 1997), although we also note that a number of constraints need to be considered before it can serve as a viable prognostic closure in ocean models (see e.g. Marshall et al., 2012). Here, we compute the PV diffusivity only as a diagnostic, and we emphasize that this choice is primarily motivated because a GM diffusivity diagnostic is not unambiguously defined in our simulations.

As discussed in C a planetary PV flux diffusion implies a thickness flux

$$(\mathbf{u}_g h)_{sgs} = -\kappa_{pv} \nabla \tilde{h}_{pv}, \quad (16)$$

where κ_{pv} is the eddy PV diffusivity coefficient, and

$$\nabla \tilde{h}_{pv} = \left(\frac{d\tilde{h}}{dx}, \frac{d\tilde{h}}{dy} - \frac{\beta \tilde{h}}{\tilde{f}} \right) \quad (17)$$

is a modified thickness gradient. Here, β is the meridional gradient of the filtered Coriolis parameter \tilde{f} , and we assumed that variations of f within the filtering scale are negligible (see Appendix C).

Following equation (16), we parameterize the time-integrated and zonally integrated SGS geostrophic volume transport (shown in Figure 10) as a function of the time-averaged and zonally averaged modified thickness gradient (17). Notice that the β term in the modified thickness gradient is relatively small, and hence, qualitatively similar results to those presented below are obtained for a pure thickness diffusivity (c.f. Zhao & Vallis, 2008). In the absence of bottom topography, and noting that we are here solving for a vertically constant thickness diffusivity, the thickness diffusivity can moreover be reinterpreted as a GM diffusivity. In the presence of bottom topography, the relationship with the GM diffusivity, however, is not straightforward.

4.3.2. Diagnosed Eddy Diffusivity

In this section, we diagnose the effective planetary PV eddy diffusivity using a least squares method, where time and spatial averaging is performed because the local correlations between standing SGS eddy transport and PV gradients are very noisy. We also clip very large values of the denominator in the diffusivity calculation (which mostly happens at small thickness height h near boundaries) to reduce unrealistic influence of boundary points on the averaged eddy diffusivity. In the next section, we will model the diagnosed eddy diffusivity via mixing length theory using the diagnosed SGS velocity as a function of filter scale.

Using a least squares approach, we diagnose the mean eddy diffusivities, separately for the regions of easterly and westerly winds, as (see Appendix D for more information)

$$\kappa_{pv} = -\frac{\langle\langle\langle (\mathbf{u}_g h)_{sgs} \cdot \nabla \tilde{h}_{pv} \rangle\rangle\rangle}{\langle\langle\langle \nabla \tilde{h}_{pv} \cdot \nabla \tilde{h}_{pv} \rangle\rangle\rangle}. \quad (18)$$

In the presence of bottom topography or continents, we also compute the transient and standing components of the planetary PV diffusivity as in (18) but using the transient and standing components of the SGS geostrophic volume transport.

In the easterly wind region of the channel configurations, the diagnosed diffusivity increases from zero, for $\Delta_f \equiv \Delta$, up to around 600 [m²/s] at $\Delta_f \sim 4^\circ$, where the scale of the eddies is fully encompassed. Above this scale, the diffusivity plateaus (Figures 12b and 12d). The diagnosed diffusivity in the easterly wind region of the Neverworld configuration behaves similarly to that in the channel configurations, albeit with smaller values: The diffusivity increases up to around 350 [m²/s] when the filter scale $\Delta_f = 3.75^\circ$, and plateaus around 400 [m²/s] for larger filter widths. Notice that we mask out regions near the continental boundaries in the Neverworld configuration since the filtering approach becomes poorly defined at the boundaries (see 4.1). As a result we are missing some of the most energetic regions, where eddy diffusivities may be large. Overall, the diffusivities in the easterly wind regions of all configurations show qualitatively similar results, where κ_{pv} increases with the filter scale up to $\sim 4^\circ$ where it plateaus. As with the fluxes, the diffusivity is dominated by the transient component in the easterly wind region in all configurations, although the standing component in the Neverworld configuration increases with filter width and becomes important at large filter scales, likely due to the importance of large-scale geostrophic flows supported by lateral boundaries (see blue diamonds in Figure 12f).

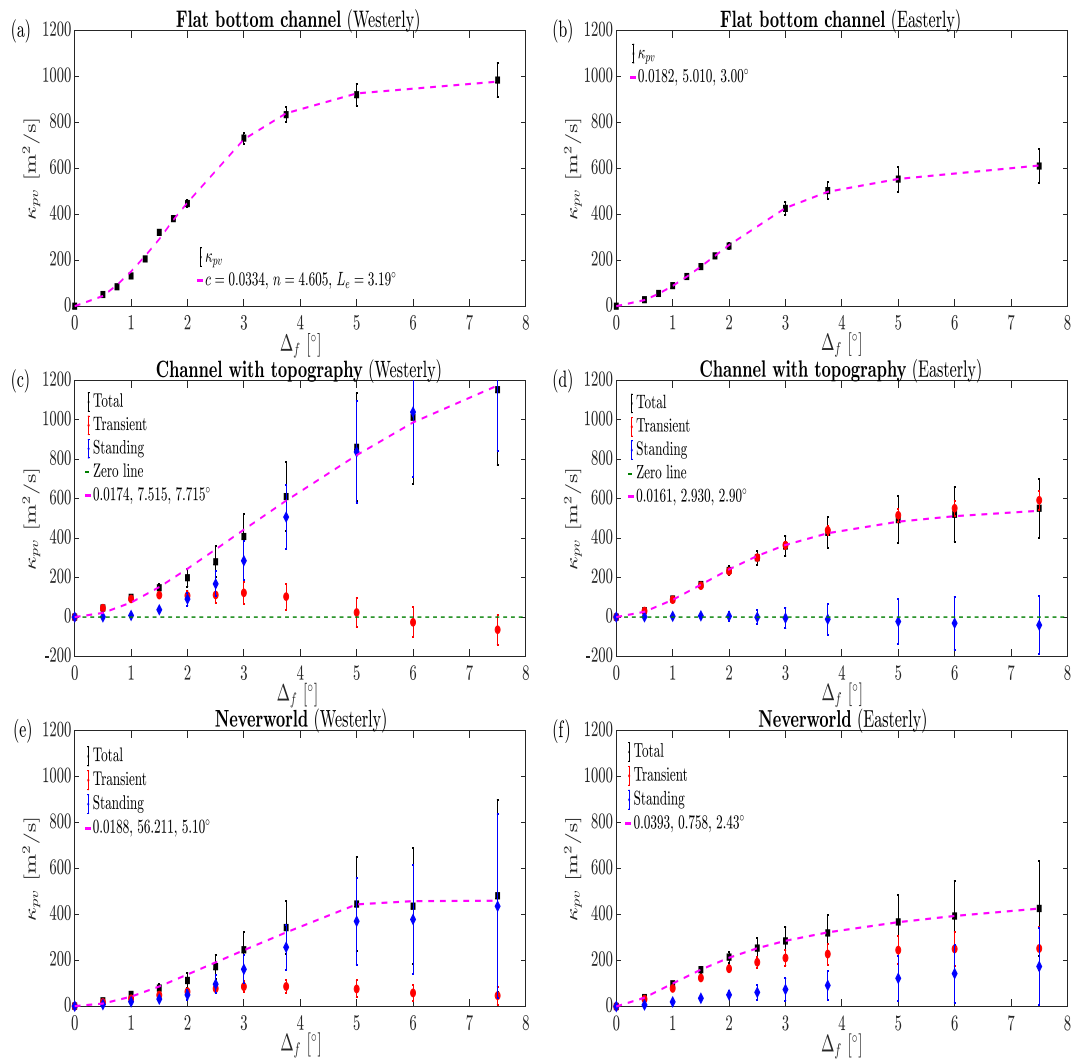


Figure 12. Diagnosed volume-averaged planetary PV diffusivity versus filter width with westerly wind (left panels) and easterly wind (right panels) for (a, b) flat bottom channel, (c, d) channel with bottom topography, and (e, f) Neverworld. Easterly and westerly winds include regions with latitudes $\theta \geq -33.3^\circ$ and $\theta < -33.3^\circ$, respectively (in Neverworld, however, the westerly region is restricted to $\theta < -50^\circ$ to remove the effects of continent on the filtered variables). The magenta dashed lines show the modeled diffusivity using a mixing length theory based on the SGS velocity and harmonic mean length scales, where the numbers given in the legend represent the fitted parameter values for c , n and L_e , respectively (see section 5). Time averaging is performed over the last 10 years of simulations.

In the westerly wind region, the diagnosed eddy diffusivity shows different dynamics in the presence or absence of topography (or continents). In the presence of topography and land, the transient component of the diffusivity is important at small scales when $\Delta_f \lesssim 2^\circ$. However, the standing contribution becomes dominant at larger filter scales as standing meanders are not fully resolved (see Figures 12c and 12e). In the flat bottom channel, the diagnosed PV diffusivity in the westerly wind region is similar to that with easterly wind stress since the transport is entirely due to transient eddies.

5. Eddy Diffusivity Parameterization

We can model an eddy diffusivity based on a velocity scale and a length scale through a mixing length argument. In this section, we try to model the planetary PV diffusivity using the SGS velocity v_{sgs} , and an effective mixing length given by a function of the filter width Δ_f and an effective eddy scale L_e , written as

$$\kappa_{pv} = cv_{sgs}L_m, \quad (19)$$

where

$$L_m = \left(\frac{1}{\Delta_f^n} + \frac{1}{L_e^n} \right)^{-1/n}, \quad (20)$$

and c is a nondimensional coefficient. The mixing length proposed in equation (20) provides a length scale that is limited by the minimum of the filter and effective eddy scales Δ_f and L_e , with a smooth transition from one limiter to another. The parameter n determines how smooth that transition is: A smaller n gives a smoother transition, while for very large n the function simply returns the minimum of the two length scales. Using the diagnosed eddy diffusivity values, we optimize parameters c , n , and L_e , such that the squared errors between the modeled and diagnosed eddy diffusivities are minimized.

The diffusivity modeled in the form of equation (19) provides a good fit to the diagnosed planetary PV diffusivities (magenta dashed lines in Figure 12), although the optimized parameters (provided in the legend of Figure 12) differ significantly between the different configurations and regions. In the easterly wind region, where the transient component of the PV diffusivity is dominant, the PV diffusivity parameterization agrees particularly well with the diagnosed PV diffusivity. In this region, the optimized value for $L_e \approx 3^\circ$, which is close to the scale of the eddies (see Figures 12b, 12d, and 12f). The nondimensional coefficient c in the easterly region is roughly similar for the two channel configurations, but it is around twice as large in the Neverworld configuration.

In the westerly region, where the standing component is dominant in configurations with topography and/or land, the agreement between the parameterized and diagnosed PV diffusivities is also good, but less perfect than for the easterly region (Figure 12). The best fit effective eddy scale L_e in the westerly regions of the flat bottom channel is again similar to the scale of transient eddies, but it is significantly larger ($\sim 5^\circ$) in the channel with topography and larger still in the Neverworld configuration ($\sim 8^\circ$). The larger maximum mixing length appears to be a result of the role of SGS standing eddies and meanders, which include a much wider range of scales (see Figures 12c and 12e).

Overall, our results suggest that the eddy diffusivity parameterization based on mixing length theory, with the diagnosed SGS velocity and a mixing length modeled as a harmonic mean of the filter scale and a maximum “eddy” scale, is a robust approach to model the eddy diffusivity through a wide range of filter scales. That is, the diagnosed eddy diffusivity for various ocean bathymetries is predicted well by a mixing length hypothesis through an *a priori* study (Figure 12). However, the optimized coefficients and parameters (including the nondimensional ones) vary between model configurations and regions, suggesting that they are not universal. A more elaborate hypothesis is therefore needed to develop a generalized parameterization. It appears that such a generalized proposition needs to account for the role of topography and how it affects eddy transports in different flow regimes (such as easterly versus westerly winds).

6. Conclusions

SGS volume fluxes in a hierarchy of idealized eddy-resolving ocean simulations are studied in this paper by introducing a spatial horizontal filtering approach. By applying different filter scales to the results of eddy-resolving simulations, we diagnose the SGS volume transport, velocity, and effective eddy diffusivity, all as a function of scale. We show that in the presence of bottom topography or continental barriers, the SGS volume transport is strongly influenced by standing meanders.

In the presence of topography, we find substantial differences in the characteristics of eddy fluxes between regions of westerly and easterly winds; transient eddies are dominant in the easterly region while standing meanders dominate regions with westerly wind. An important consequence of the presence of SGS standing meanders is that the vertical sum of the zonally averaged SGS volume transport does not integrate to 0. In this case, diagnostics based on isopycnal height diffusion are not well defined. To proceed, we use a planetary PV diffusivity model to parameterize SGS volume transport. In the region with easterly wind, the transient PV diffusivity increases with filter width and converges above $\Delta_f \gtrsim 4^\circ$. In the region with westerly wind, SGS transient eddies are important when $\Delta_f < 1^\circ$, while the SGS standing meanders become dominant when $\Delta_f \gtrsim 1^\circ$. We speculate that the diverging characteristics of eddy fluxes in the easterly versus westerly regions are due to different vertical mode structures: Deeper modes that are strongly affected by bottom topography

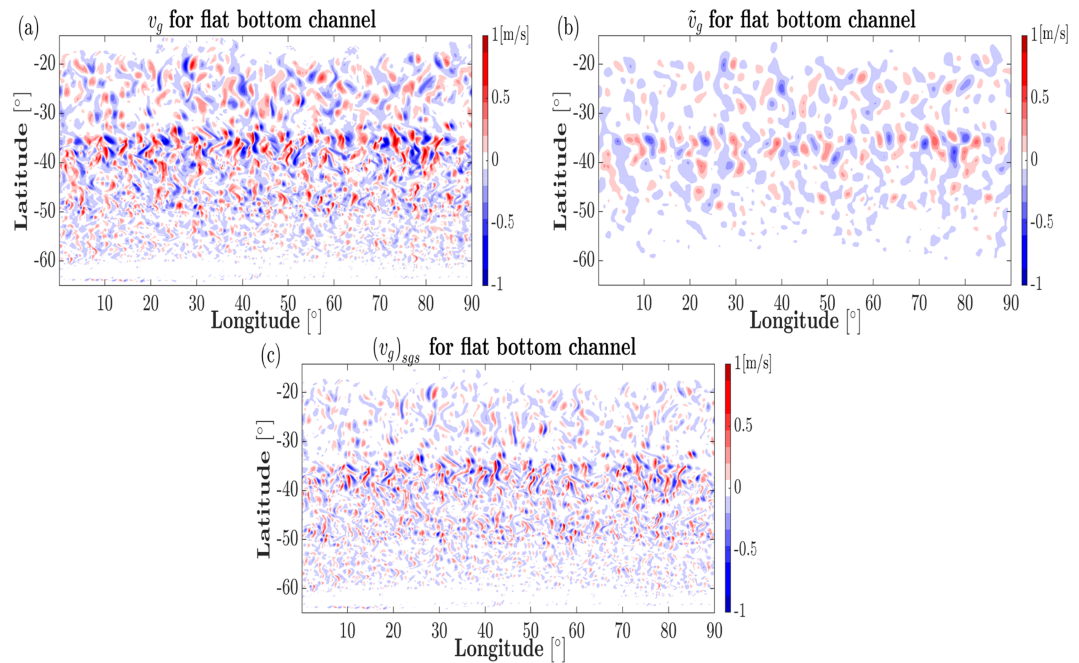


Figure A1. Meridional geostrophic velocity snapshot ($t = 75$ [yr]) at the surface layer for the flat bottom channel case: (a) unfiltered, (b) filtered and (c) SGS fields. The filter scale is $\Delta_f = 2^\circ$.

are expected in the relatively weakly stratified westerly wind region, while shallower and surface intensified modes are expected in the easterly wind region (see e.g. Tulloch et al., 2011). Our results suggest that the wind stress direction affects SGS fluxes, and hence, SGS parameterizations in General Circulation Models may need to consider these effects.

Moreover, we show that we can model the diagnosed SGS planetary PV diffusivity using mixing length theory with the SGS velocity scale and a blend of the filter scale Δ_f and effective eddy scale L_e . The optimized eddy scale L_e is around the scale of the transient eddies in easterly regions, while the optimized L_e seems to be significantly larger due to the effect of standing meanders in westerly regions of configurations with topography and/or land. We therefore suggest that the mixing length hypothesis provides a promising route toward a diffusive closure, although a theory to predict the various model coefficients is still needed.

Appendix A: Examples of Filtered Fields

Figure A1 shows the unfiltered, filtered, and SGS fields of meridional geostrophic velocity in the surface layer for the flat bottom channel configuration when $\Delta_f = 2^\circ$. The filtered part of the meridional velocity includes mostly large-scale motions that are resolved by the filter scale $\Delta_f = 2^\circ$, while the SGS part includes small-scale structures that are below the filter width, and whose effects would therefore need to be parameterized in coarser resolution simulations.

Appendix B: SGS Form Stress

We can write the meridional geostrophic volume transport in the following form

$$\int_{z_b}^0 v_g dz = \int_{z_b}^0 \frac{1}{\rho_0 f} \frac{\partial p}{\partial x} dz, \quad (B1)$$

where ρ_0 , p , f , and z are the reference density, pressure, Coriolis parameter, and vertical direction, respectively. Variables at the bottom of the ocean are shown with subscript b , where $z_b = z_b(x, y)$ is not constant in configurations with bottom topography. Taking a zonal integral over a reentrant domain and simplifying

the right-hand side of equation (B1) using the Leibniz integral rule, we can write

$$\int \left(\int_{z_b}^0 v_g dz \right) dx = - \int \left(\frac{1}{\rho_0 f} p_b(x, y) \frac{\partial z_b(x, y)}{\partial x} \right) dx. \quad (\text{B2})$$

In stacked shallow water model, equation (B2), can be written as follows

$$\left\langle \sum_{i=1}^N v_g^i h^i \right\rangle = \frac{1}{f} \left\langle M_b \frac{\partial z_b}{\partial x} \right\rangle, \quad (\text{B3})$$

where $M_b = \sum_{i=1}^N g^i \eta^i$ is the Montgomery potential in the bottom model layer and the angle bracket sign $\langle \cdot \rangle$ denotes a zonal average (and we again assume a zonally reentrant domain). By filtering equation (B3), we can get

$$\left\langle \widetilde{\sum_{i=1}^N v_g^i h^i} \right\rangle = \frac{1}{f} \left\langle \widetilde{M_b \frac{\partial z_b}{\partial x}} \right\rangle, \quad (\text{B4})$$

where we neglected contributions associated with variations in the Coriolis parameter f over the filter stencil, and we have used that the filtering operator is linear. Similarly, the zonally averaged filter-resolved meridional geostrophic transport can be written as follows

$$\left\langle \widetilde{\sum_{i=1}^N \tilde{v}_g^i \tilde{h}^i} \right\rangle = \frac{1}{f} \left\langle \widetilde{M_b \frac{\partial z_b}{\partial x}} \right\rangle, \quad (\text{B5})$$

where we have assumed that the filtering operator commutes with the differentiation operator. This commutation does not hold exactly for our filtering operator, but it is a very good approximation away from boundaries (and hence in the zonally reentrant channel configuration).

If we subtract equation (B5) from (B4), we find that

$$\left\langle \widetilde{\sum_{i=1}^N (v_g^i h^i)}_{\text{sgs}} \right\rangle = \frac{1}{f} \left\langle \left(M_b \frac{\partial z_b}{\partial x} \right)_{\text{sgs}} \right\rangle, \quad (\text{B6})$$

which indicates that the vertical sum of the meridional volume transport is balanced by the SGS form drag, where

$$\left(M_b \frac{\partial z_b}{\partial x} \right)_{\text{sgs}} = \widetilde{M_b \frac{\partial z_b}{\partial x}} - \widetilde{M_b \frac{\partial z_b}{\partial x}}. \quad (\text{B7})$$

Appendix C: Relating PV Diffusion to Thickness Fluxes

We start by assuming a diffusive closure for the thickness weighted eddy PV flux:

$$(\mathbf{u}_g q)^*_{\text{sgs}} = -\kappa_{pv} \nabla \tilde{q}^*, \quad (\text{C1})$$

where $q = (f + \zeta)/h$, f , and ζ are the planetary and relative vorticities, respectively, $(\tilde{\cdot})^* = \widetilde{h \cdot}/\tilde{h}$ denotes a thickness weighted filtering, and $(\mathbf{u}q)^*_{\text{sgs}} = \widetilde{\mathbf{u}q}^* - \widetilde{\mathbf{u}}^* \tilde{q}^*$ is the corresponding SGS flux. For a Reynolds averaging, a downgradient flux closure for the thickness weighted isopycnal eddy PV flux can be motivated based on an analysis of the PV variance budget (Jansen & Ferrari, 2013; Marshall et al., 1999). Our LES filter is not a Reynolds average, and hence, it is less clear in how far a diffusive closure can be justified. Nevertheless, noting the wide application of diffusive closures in general circulation modes, we here use it as a reasonable starting point.

It is a common assumption that (away from the western boundary) the gradient and flux of the relative vorticity contribution to the PV are small, such that we can approximate $q \approx f/h$ (see e.g. Abernathey et al., 2010; Smith, 2007; Tulloch et al., 2011). This assumption is likely to hold well at large filter scales, although it is less clear how well it holds at smaller scales where localized jets with significant relative vorticity can be resolved. A comprehensive treatment of volume and momentum fluxes (as suggested by e.g. Bachman et al., 2017) may be needed in this limit, but such an approach is beyond the scope of this study.

Using a planetary PV approximation, the left-hand side of equation (C1) can be approximated as

$$(\mathbf{u}_g q)_{sgs}^* \approx \left(\frac{\widetilde{u_g f}}{h} \right)^* - \widetilde{u_g}^* \left(\frac{\widetilde{f}}{h} \right)^* = \frac{\widetilde{u_g f}}{\tilde{h}} - \frac{\widetilde{u_g h} \tilde{f}}{\tilde{h}^2}, \quad (C2)$$

while the right-hand side of equation (C1) becomes

$$-\kappa_{pv} \nabla \tilde{q}^* \approx -\kappa_{pv} \nabla \left(\frac{\tilde{f}}{h} \right)^* = -\kappa_{pv} \nabla \left(\frac{\tilde{f}}{\tilde{h}} \right), \quad (C3)$$

Using equations (C1, C2, C3), we can write the meridional flux as

$$\frac{\widetilde{v_g f}}{\tilde{h}} - \frac{\widetilde{v_g h} \tilde{f}}{\tilde{h}^2} = -\kappa_{pv} \left(\frac{\beta}{\tilde{h}} - \frac{\tilde{f}}{\tilde{h}^2} \frac{d\tilde{h}}{dy} \right), \quad (C4)$$

where $\beta = d\tilde{f}/dy \approx df/dy$. Substituting $\widetilde{v_g h} = \tilde{v}_g \tilde{h} + (v_g h)_{sgs}$ in equation (C4), we obtain the following equation for the SGS meridional volume transport

$$(v_g h)_{sgs} = -\kappa_{pv} \left(\frac{d\tilde{h}}{dy} - \frac{\beta \tilde{h}}{\tilde{f}} \right) + \left(\frac{\widetilde{v_g f}}{\tilde{f}} \tilde{h} - \tilde{v}_g \tilde{h} \right). \quad (C5)$$

Assuming that variations of the Coriolis parameter on the scale of the filter are negligible, such that $\widetilde{v_g f} \approx \tilde{v}_g \tilde{f}$, the second parenthesis on the right-hand side of equation (C5) is approximately zero. As a result, we can write

$$(v_g h)_{sgs} \approx -\kappa_{pv} \left(\frac{d\tilde{h}}{dy} - \frac{\beta \tilde{h}}{\tilde{f}} \right). \quad (C6)$$

Similarly, we find for the SGS zonal volume transport

$$(\mathbf{u}_g h)_{sgs} = -\kappa_{pv} \frac{d\tilde{h}}{dx}. \quad (C7)$$

That is, a diffusive closure for the thickness weighted planetary PV flux leads to a thickness flux downgradient of a modified thickness with a contribution from the planetary vorticity gradient:

$$\nabla \tilde{h}_{pv} = \left(\frac{d\tilde{h}}{dx}, \frac{d\tilde{h}}{dy} - \frac{\beta \tilde{h}}{\tilde{f}} \right). \quad (C8)$$

Appendix D: Least Squares Approach

To estimate the planetary PV diffusivity in the thickness flux equation

$$(\mathbf{u}_g h)_{sgs} = -\kappa_{pv} \nabla \tilde{h}_{pv}, \quad (D1)$$

we use a least squares approach to minimize the error

$$Q = \left((\mathbf{u}_g h)_{sgs} + \kappa_{pv} \nabla \tilde{h}_{pv} \right)^2. \quad (D2)$$

Setting $\partial Q / \partial k_{pv} = 0$ yields a regression equation for the optimized PV diffusivity:

$$\kappa_{pv} = -\frac{(\mathbf{u}_g h)_{sgs} \cdot \nabla \tilde{h}_{pv}}{\nabla \tilde{h}_{pv} \cdot \nabla \tilde{h}_{pv}}. \quad (D3)$$

D.1. Confidence Interval

Confidence intervals in Figures 8, 9, and 12 are computed using an effective number of freedom set by the filter scale. Let us assume D is found using the least squares approach for parameterizing a dependent variable \mathbf{y} in terms of an independent variable \mathbf{x} (i.e., $\mathbf{y} = \mathbf{D}\mathbf{x}$). We can calculate the standard error for the least square approach as follows

$$Er = \frac{\sqrt{\sum (y_i - Dx_i)^2 / N}}{\sqrt{\sum (x_i - \bar{x}_i)^2}}, \quad (D4)$$

where \bar{x} is the mean of \mathbf{x} , and N is number of degrees of freedom. Since neighboring grid points are generally not independent (particularly noting that the regression is applied to filtered quantities), we estimate the effective number of degrees of freedom as

$$N = \frac{N_{tot}}{(\Delta_f / \Delta)^2}, \quad (D5)$$

where N_{tot} is the total number of grid points that are used in the regression, Δ_f is the filter scale, and Δ is the grid spacing of the general circulation mode. The confidence interval provided in the figures is then computed as $D \pm z^* Er$, where we use $z^* = 1.96$ for the %95 confidence interval.

Acknowledgments

This work has benefited from comments by Steve Griffies, Hussein Aluie, David Marshall, and an anonymous reviewer. This work was completed in part with resources provided by the University of Chicago Research Computing Center (RCC). Financial support was provided by National Science Foundation through Awards 1536360 and 1536450 which is gratefully acknowledged. S. K. gratefully acknowledges the hospitality of the Department of Geophysical Sciences at the University of Chicago during his visit. A. A. also acknowledges support by Award NA14OAR4320106 from the National Oceanic and Atmospheric Administration, U.S. Department of Commerce. The statements, findings, conclusions, and recommendations are those of the author(s) and do not necessarily reflect the views of the National Oceanic and Atmospheric Administration, or the U.S. Department of Commerce. All source code for generating the results are available at the GitHub (<https://github.com/sinakhani/Neverworld>, <https://doi.org/10.5281/zenodo.3560270>).

References

- Abernathey, R., & Cessi, P. (2014). Topographic enhancement of eddy efficiency in baroclinic equilibration. *Journal of Physical Oceanography*, 44, 2107–2126.
- Abernathey, R., Ferreira, D., & Klocker, A. (2013). Diagnostics of isopycnal mixing in a circumpolar channel. *Ocean Modelling*, 72, 1–16.
- Abernathey, R., Marshall, J., Mazloff, M., & Shuckburgh, E. (2010). Enhancement of mesoscale eddy stirring at steering levels in the Southern Ocean. *Journal of Physical Oceanography*, 40, 170–184.
- Aluie, H. (2019). Convolutions on the sphere: Commutation with differential operators. *International Journal on Geomathematics*, 10, 9. <https://doi.org/10.1007/s13137-019-0123-9>
- Aluie, H., Hecht, M., & Vallis, G. K. (2018). Mapping the energy cascade in the North Atlantic Ocean: The coarse-graining approach. *Journal of Physical Oceanography*, 48, 225–244.
- Bachman, S. D., Fox-Kemper, B., & Pearson, B. (2017). A scale-aware subgrid model for quasi-geostrophic turbulence. *Journal of Geophysical Research: Oceans*, 122, 1529–1554. <https://doi.org/10.1002/2016JC012265>
- Berloff, P. S. (2005). On dynamically consistent eddy fluxes. *Dynamics of Atmospheres and Oceans*, 38, 123–146.
- Berloff, P. S. (2018). Dynamically consistent parameterization of mesoscale eddies. Part III: Deterministic approach. *Ocean Modelling*, 127, 1–15.
- Danabasoglu, G., & Marshall, J. (2007). Effects of vertical variations of thickness diffusivity in an ocean general circulation model. *Ocean Modelling*, 18, 122–141.
- Ferrari, R., & Nikurashin, M. (2010). Suppression of eddy diffusivity across jets in the Southern Ocean. *Journal of Physical Oceanography*, 40, 1510–1519.
- Fox-Kemper, B., & Menemenlis, D. (2008). Can large eddy simulation techniques improve mesoscale rich ocean models. In M. W. Hecht, & H. Hasumi (Eds.), *Ocean Modeling in an Eddying Regime* (Vol. 177, pp. 319–337). Washington, DC: Geophysical Monograph Series.
- Gent, P. R., & McWilliams, J. C. (1990). Isopycnal mixing in ocean circulation model. *Journal of Physical Oceanography*, 20, 150–155.
- Greatbatch, R. J. (1998). Exploring the relationship between eddy-induced transport velocity, vertical momentum transfer, and the isopycnal flux of potential vorticity. *Journal of Physical Oceanography*, 28, 422–432.
- Hallberg, R. (2013). Using a resolution function to regulate parameterizations of oceanic mesoscale eddy effects. *Ocean Modelling*, 72, 92–103.
- Hallberg, R., & Gnanadesikan, A. (2006). The role of eddies in determining the structure and response of the wind-driven Southern hemisphere overturning: Results from the modeling eddies in the Southern ocean (MESO) project. *Journal of Physical Oceanography*, 36, 2232–2252.
- Jansen, M., & Ferrari, R. (2013). The vertical structure of the eddy diffusivity and the equilibration of the extratropical atmosphere. *Journal of the Atmospheric Sciences*, 70(5), 1456–1469.
- Johnson, G. C., & Bryden, H. L. (1989). On the size of the Antarctic Circumpolar Current. *Deep Sea Research Part A. Oceanographic Research Papers*, 36(1), 39–53.
- Khani, S., & Waite, M. L. (2016). Backscatter in stratified turbulence. *European Journal of Mechanics - B/Fluids*, 60, 1–12.
- Khani, S., & Waite, M. L. (2015). Large eddy simulations of stratified turbulence: The dynamic Smagorinsky model. *Journal of Fluid Mechanics*, 773, 327–344.
- Leith, C. E. (1996). Stochastic models of chaotic systems. *Physica D: Nonlinear Phenomena*, 98, 481–491.
- Marshall, D. P., Maddison, J. R., & Berloff, P. S. (2012). A framework for parameterizing eddy potential vorticity fluxes. *Journal of Physical Oceanography*, 42, 539–557.
- Marshall, D. P., Williams, R. G., & Lee, M. M. (1999). The relation between eddy-induced transport and isopycnal gradients of potential vorticity. *Journal of Physical Oceanography*, 29, 1571–1578.
- Mazloff, M. R., Ferrari, R., & Schneirder, T. (2013). The force balance of the Southern Ocean meridional overturning circulation. *Journal of Physical Oceanography*, 43, 1193–1208.
- McWilliams, J. C. (2008). *The nature and consequence of oceanic eddies*. Geophysical Monograph Series (Vol. 177, pp. 5–15). Washington, DC: American Geophysical Union.

- Moeng, C.-H., & Sullivan, P. P. (1994). A comparison of shear- and buoyancy-driven planetary boundary layer flows. *Journal of the Atmospheric Sciences*, 51(7), 992–1022.
- Porté-Agel, F., Meneveau, C., & Parlange, M. (2000). A scale-dependent dynamic model for large-eddy simulation: Application to a neutral atmospheric boundary layer. *Journal of Fluid Mechanics*, 415, 261–284.
- Sadek, M., & Aluie, H. (2018). Extracting the spectrum of a flow by spatial filtering. *Physical Review Fluids*, 3, 124610.
- Smagorinsky, J. (1963). General circulation experiments with the primitive equations. *Monthly Weather Review*, 91, 99–164.
- Smith, K. S. (2007). The geography of linear baroclinic instability in Earth's oceans. *Journal of Marine Research*, 39(5), 655–683.
- Smith, K. S., & Marshall, J. (2009). Evidence for enhanced eddy mixing at middepth in the Southern Ocean. *Journal of Physical Oceanography*, 39, 50–69.
- Soufflet, Y., Marchesiello, P., Lemarié, F., Jouanno, J., Capet, X., Debreu, L., & Benshila, R. (2016). On effective resolution in ocean models. *Ocean Modelling*, 98, 36–50.
- Thompson, A. F. (2008). The atmospheric ocean: Eddies and jets in the Antarctic Circumpolar Current. *Philosophical Transactions of the Royal Society A*, 366, 4529–4541.
- Treguier, A. M., Held, I., & Larichev, V. D. (1997). Parameterization of quasigeostrophic eddies in primitive equation ocean model. *Journal of Physical Oceanography*, 27, 567–580.
- Treguier, A. M., & McWilliams, J. C. (1990). Topographic influences on wind-driven, stratified flow in a β -plane channel: An idealized model for the Antarctic Circumpolar Current. *Journal of Physical Oceanography*, 20, 321–343.
- Tulloch, R., Marshall, J., Hill, C., & Smith, K. S. (2011). Scales, growth rates, and spectral fluxes of baroclinic instability in the ocean. *Journal of Physical Oceanography*, 41, 1057–1076.
- Visbeck, M., Marshall, J., Haine, T., & Spall, M. (1997). Specification of eddy transfer coefficients in coarse-resolution ocean circulation models. *Journal of Physical Oceanography*, 27, 381–402.
- Wolff, J.-O., Maier-Reime, E., & Olbers, D. J. (1991). Wind-driven flow over topography in a zonal β -plane channel: A quasi-geostrophic model of the Antarctic Circumpolar Current. *Journal of Physical Oceanography*, 21, 236–264.
- Zhao, R., & Vallis, G. (2008). Parameterizing mesoscale eddies with residual and Eulerian schemes, and a comparison with eddy-permitting models. *Ocean Modelling*, 23, 1–12.